A national laboratory of the U.S. Department of Energy
Office of Energy Efficiency & Renewable Energy

National Renewable Energy Laboratory

Innovation for Our Energy Future

Development of Automated Production Line Processes for Solar Brightfield Modules

Final Annual Technical Progress Report 1 July 2004 — 15 October 2005

M.J. Nowlan, J.M. Murach, S.F. Sutherland, D.C. Miller, S.B. Moore, and S.J. Hogan
Spire Corporation
Bedford, Massachusetts

Subcontract Report
NREL/SR-520-40406
August 2006

NREL is operated by Midwest Research Institute • Battelle Contract No. DE-AC36-99-GO10337

Development of Automated Production Line Processes for Solar Brightfield Modules

Final Annual Technical Progress Report 1 July 2004 — 15 October 2005

M.J. Nowlan, J.M. Murach, S.F. Sutherland, D.C. Miller, S.B. Moore, and S.J. Hogan
Spire Corporation
Bedford, Massachusetts

NREL Technical Monitor: B. Keyes
Prepared under Subcontract No. ZDO-3-30628-12

Subcontract Report
NREL/SR-520-40406
August 2006

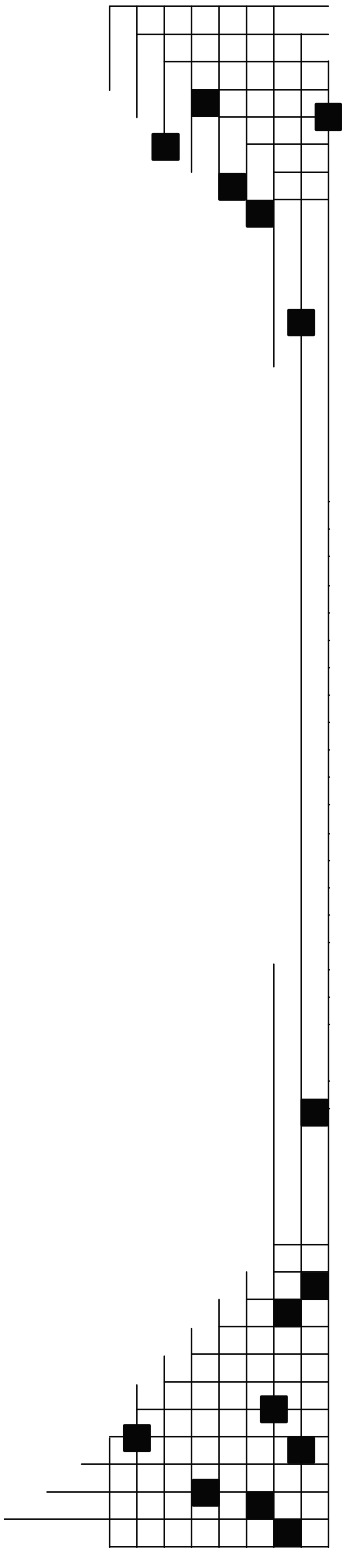

National Renewable Energy Laboratory
1617 Cole Boulevard, Golden, Colorado 80401-3393
303-275-3000 • www.nrel.gov

Operated for the U.S. Department of Energy
Office of Energy Efficiency and Renewable Energy
by Midwest Research Institute • Battelle

Contract No. DE-AC36-99-GO10337

TABLE OF CONTENTS

LIST OF ILLUSTRATIONS

LIST OF TABLES

1 INTRODUCTION

This is Spire Corporation's Annual Technical Progress Report for Phase 2 of a program entitled "Development of Automated Production Line Processes for Solar Brightfield Modules." This program is supported by the U. S. Department of Energy under the National Renewable Energy Laboratory's Photovoltaic Manufacturing R&D (PVMRD) project. Phase 2 efforts extended from July 1, 2004 to October 15, 2005.

1.1 Objective

Spire is addressing the PVMRD project goals of improving PV manufacturing processes and products while reducing costs and providing a technology foundation that supports significant manufacturing scale-up. To accomplish this, we are focusing our efforts on the design of a large area utility-scale module and the development of the necessary manufacturing techniques and equipment to manufacture such a module in a high-volume production environment.

1.2 Approach

A three-phase program is underway for developing and demonstrating new automated systems for fabricating very large photovoltaic (PV) modules ideal for use in multi-megawatt grid-connected applications. We designed a large area (1.57 m x 3.68 m) 800 W module and we are developing associated module production equipment that will minimize the total installed system cost for utility-scale PV arrays. Activities in Phase 2 focused on the development of automation for module materials lay-up, cell string busing, and module lamination; enhancements to the cell stringing and lamination processes; and performance testing of large area modules. Program tasks are listed in Table 1.

Table 1 Program tasks.

Phase	Term	Task
1	June 2003 through June 2004	1 Design Brightfield Module and Production Line 2 Develop Cell String Inspection Process 3 Develop Advanced Lamination Process 4 Design Module Lay-up System 5 Design String Busing System
2	July 2004 through October 2005	6 Fabricate & Test Module Lay-up System 7 Fabricate & Test String Busing System 8 Design Advanced Lamination Process Tool 9 Design Lamination Automation 10 Design Large Area Solar Simulator 11 Develop Soldering Process for Thin Solar Cells
3	October 2005 through December 2006	12 Fabricate & Test Advanced Laminator 13 Fabricate & Test Laminator Automation 14 Fabricate & Test Large Area Solar Simulator 15 Develop Computer Integrated Manufacturing System

Spire partnered with the Automation & Robotics Research Institute (ARRI) at the University of Texas at Arlington (UTA), a lower-tier subcontractor, in Phases 1 and 2. In Phase 2, ARRI provided process support for automated bus and diode soldering under Task 7.

2 TECHNICAL DISCUSSION

2.1 Task 6 – Fabricate and Test Module Lay-up System

In Task 6 we demonstrated a new automated system for assembling module materials for lamination. Spire and the Automation & Robotics Research Institute (ARRI) worked with Rosenthal Manufacturing to define a system that is customized to handle the lay-up process requirements for Spire's Brightfield module. We specified a system with the capacity for handling material up to 72 inches wide, large enough to handle our 62 inch wide module glass.

The custom lay-up system, shown in Figure 1, is capable of feeding, cutting to length, and placing two different sheet materials (encapsulant and back sheet) simultaneously. The material feed system is synchronized with a servomotor-driven module conveyor to place the sheet materials directly on the module. An in-line punch feature was designed and installed to punch a rectangular cutout along one edge of the sheet for feeding bus leads through to the module output boxes. The system can also dispense a single layer of material, with the punch feature disabled, to place the first layer of encapsulant on the glass sheet, prior to placing the solar cell strings.

05-091WA

Figure 1 Automated module lay-up system.

The system was tested with ethylene vinyl acetate (EVA) encapsulant sheet and Tedlar[1]-polyester-EVA (TPE) back sheet. Both the EVA and the TPE ran successfully through the system, including feeding, punching, cutting, and placing. Repeatability data was measured for material length, punched hole location, and placement on a moving substrate, such as a glass sheet that forms a module front surface. Since the back sheet has low elongation, it did not stretch during unwinding and feeding, and the dimensional variation was within ±0.75 mm (see Table 2). Similar data measured for EVA shows higher variation, up to ±3 mm, due to the elastic nature of the material (Table 3).

Table 2 **Dimensional variations in sheet placement, cut length, and punch locations for nominal 2540 mm long TPE sheets.**

	Placement (mm)		Length (mm)		Location (mm)	
Run #	Left	Right	Left	Right	Punch #1	Punch #2
1	461.0	462.0	2542.0	2542.0	9.0	2448.0
2	462.5	461.0	2541.5	2542.0	8.0	2447.5
3	462.5	462.0	2542.0	2541.5	8.0	2447.5
4	462.5	462.0	2541.0	2541.5	8.0	2447.5
5	462.0	462.0	2541.5	2541.0	8.5	2447.0
6	462.0	462.0	2542.0	2542.0	8.0	2447.5
Average	462.1	461.8	2541.7	2541.7	8.3	2447.5
Max - min	1.5	1.0	1.0	1.0	1.0	1.0

Table 3 **Dimensional variations in sheet placement, cut length, and punch locations for nominal 2540 mm long EVA sheets.**

	Placement (mm)		Length (mm)		Location (mm)	
Run #	Left	Right	Left	Right	Punch #1	Punch #2
1	467.0	467.0	2495.0	2496.0	12.0	2408.0
2	468.0	470.0	2494.0	2495.0	12.0	2406.0
3	466.0	467.0	2495.0	2495.0	12.0	2407.0
4	468.0	470.0	2493.0	2494.0	12.0	2406.0
5	465.0	468.0	2494.0	2495.0	13.0	2408.0
6	469.0	472.0	2494.0	2494.0	12.0	2406.0
7	469.0	470.0	2495.0	2495.0	13.0	2408.0
8	471.0	473.0	2493.0	2491.0	13.0	2405.0
9	469.0	470.0	2492.0	2493.0	13.0	2404.0
10	470.0	471.0	2493.0	2493.0	13.0	2405.0
Average	468.2	469.8	2493.8	2494.1	12.5	2406.3
Max - min	6.0	6.0	3.0	5.0	1.0	4.0

We found that EVA stretches in the machine length direction during feeding and shrinks after cutting, resulting in a length that is shorter than expected. The observed shrinkage was 1.8% of the sheet length. For the module's front EVA layer, where only one layer is being dispensed, we can compensate for the amount of shrinkage by adding this percentage to the desired length as an offset. For the back layer, the shrinkage causes misalignment in the punched holes and the cut sheet lengths between the EVA and the TPE. This problem can be solved by using an EVA-on-fiberglass material, which has much lower elongation than EVA alone. This material is a standard component used behind the cells in Spire's modules.

The lay-up machine was tested with a roll of EVA-on-fiberglass material to compare with the EVA material. The EVA-on-fiberglass ran successfully through the system, including feeding, punching, cutting, and placing. The EVA-on-fiberglass showed much less stretch during feeding than EVA without fiberglass.

Our original punch design called for a 25 mm square hole, large enough so that cut sheets could be fed from the top down over an output bus ribbon that is bent up from the surface of the module at a 90°

angle. Upon review, we realized that this results in an area with no encapsulant or back sheet behind a section of the bus ribbon and an edge of a solar cell. While a terminal box will cover the hole, the design provides inferior environmental protection for the cell and the bus ribbon.

The punch design was changed to create a slot, 3 mm wide by 16 mm long. A photo of the punched slots in EVA-on-fiberglass sheets is shown in Figure 2. With this design, the hole is narrow enough for the EVA to flow and fill in during lamination, fully encapsulating the cell and bus ribbon. To make the sheet lay-up process work with such a narrow slot, the output bus ribbon is not bent up, but lies flat on the module when the back EVA and Tedlar sheets are dispensed. The slot lines up with the flat output ribbon at the location where the ribbon feeds through. In the original design with the bent ribbon, an operator is required to press the ribbon flat after the back sheets are dispensed, prior to lamination. In the new design, an operator is required to feed the bus ribbon through the slot prior to lamination.

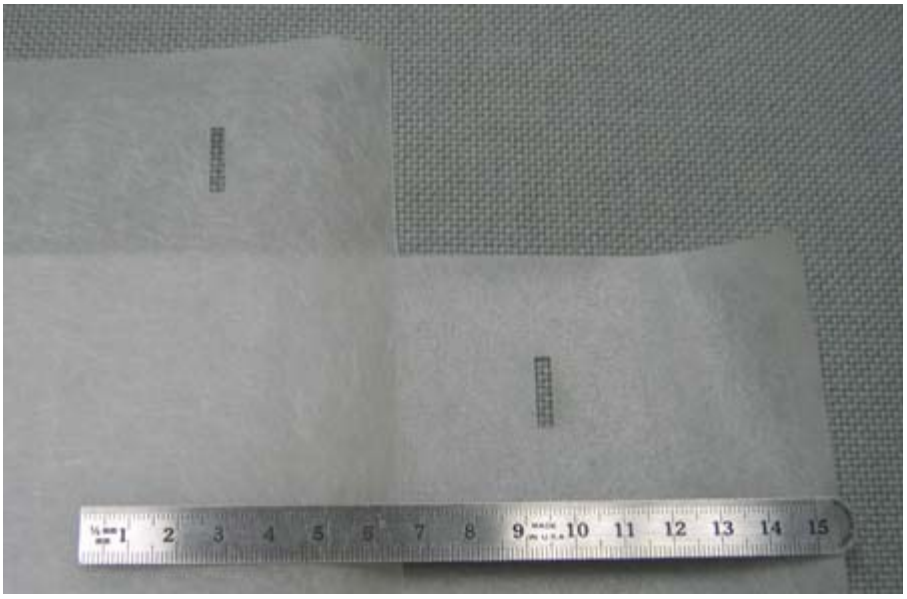

05-056WA

Figure 2 Punched slots in EVA-on-fiberglass sheet.

2.2 Task 7 – Fabricate & Test String Busing System

Engineering design work for a production prototype string busing system was completed, and the system was built and tested. The system consists of automation for transporting and aligning 5 ft x 12 ft modules, cutting and placing bus ribbon, applying flux, placing diodes, and soldering bus ribbons. Two separate systems were built, one for fabricating bus ribbons off-line, and one for installing bus ribbons and diodes in a module, on an assembly line.

2.2.1 Bus Ribbon Fabrication

Mechanical and electrical designs were completed for the bus ribbon fabrication machine, which automatically feeds ribbon from reels, straightens it to remove coil set, cuts or punches it to length, and fills a tray with a stack of ribbon. Assembly and detail drawings were completed for all system subassemblies. A view from the SolidWorks CAD model of the machine is shown in Figure 3. Electrical and pneumatics schematics were created.

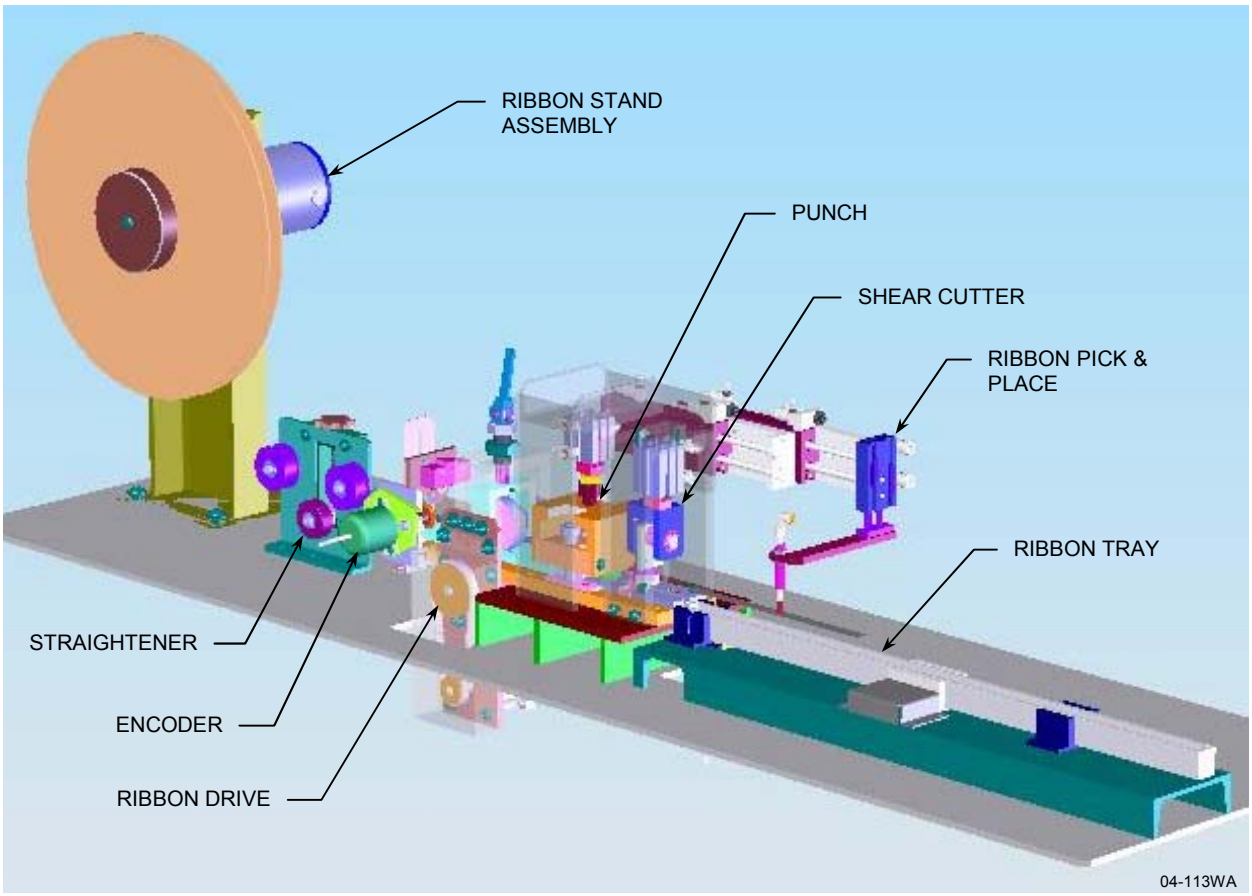

Figure 3 Ribbon fabrication machine design. Main support frame and controls cabinet not shown.

Software was written for controlling the bus ribbon fabrication machine. A Visual Basic graphical user interface (GUI) was coded and debugged. The main window is shown in Figure 4. Controls are provided for cutting ribbons continuously or in batches, selecting the number of ribbons per batch, and setting the ribbon length, feed velocity, and feed acceleration. A counter displays how many ribbons have been cut. The System section of the window displays the status of the machine sensor inputs, including end of ribbon reel, cutter and punch positions, ribbon pick-and-place positions, vacuum, and ribbon presence in the tray. Buttons are provided for manually actuating outputs for jogging (advancing) ribbon; punching, cutting, and ejecting ribbon; moving the pick-and-place actuators; and turning the pick-and-place vacuum on and off. Motor controller programs were written for automatic operation, to allow the controller to run the machine without connection to a PC if desired.

Mechanical, pneumatic, and electrical assembly work was completed, software was installed, and the machine was tested. The completed system is shown in Figure 5. Figure 6 shows a close-up view of the main components, including (left to right) the ribbon straightener (removes coil set), ribbon feed encoder (measures ribbon length), ribbon drive wheels, punch (punches a tab for the diode), knife set, pick-and-place hand, and ribbon tray.

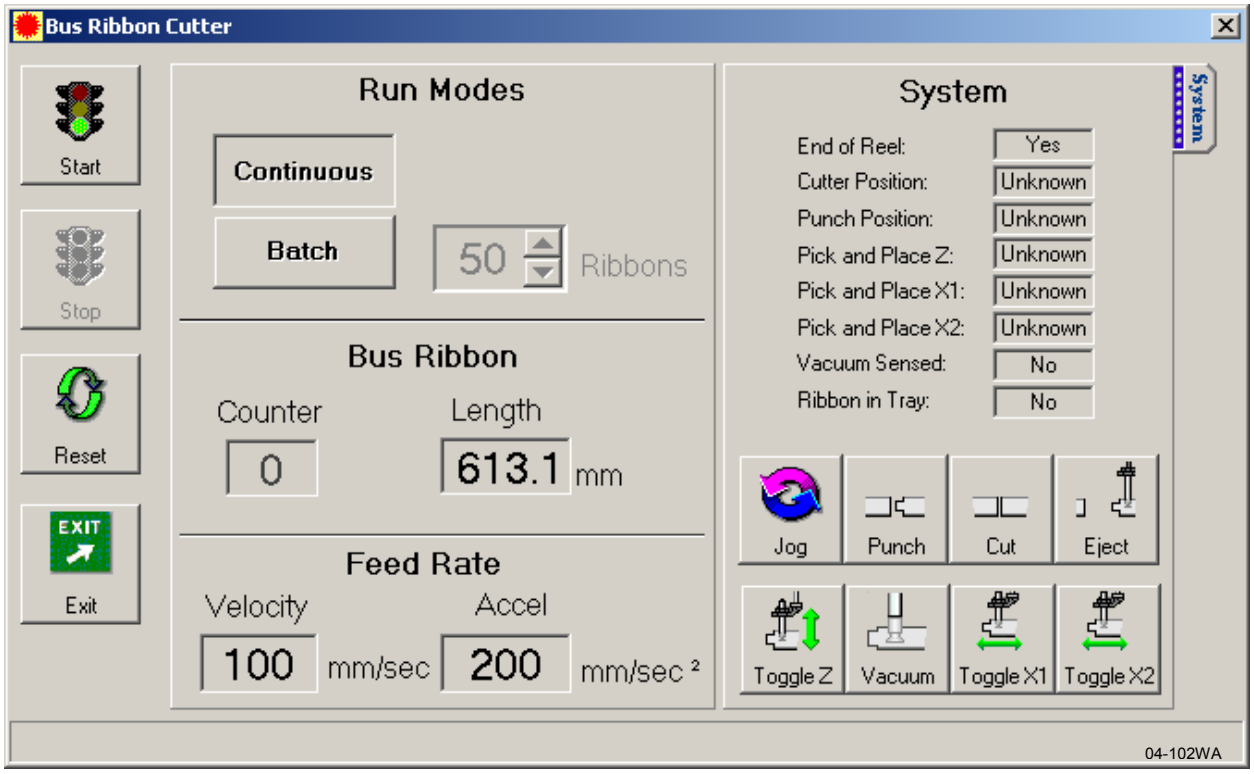

Figure 4 Main operating window for the ribbon fabrication machine.

05-092WA

Figure 5 Bus ribbon fabrication machine.

05-093WA

Figure 6 Close-up view of bus ribbon fabrication machine components.

2.2.2 Bus Ribbon and Diode Installation

Mechanical and electrical designs were completed for the bus ribbon and diode installation system, which automatically picks, aligns, and places bus ribbons and diodes, applies no-clean flux for diode soldering, and solders bus ribbons to diodes and string ribbons. Mechanical assembly and detail drawings were completed for all system subassemblies, and electrical and pneumatics schematics were created.

A large four-axis (x, y, z, and θ) Cartesian robot was specified. A CAD model of the robot is shown in Figure 7. The robot can travel 3935 mm in the x axis, 2250 mm in the y axis, and 150 mm in the z axis. Servomotors drive all four axes. The x and y axes have belt driven slides, the z axis has a lead screw, guide rods, and a brake, and the θ axis has a 127 mm diameter rotary table.

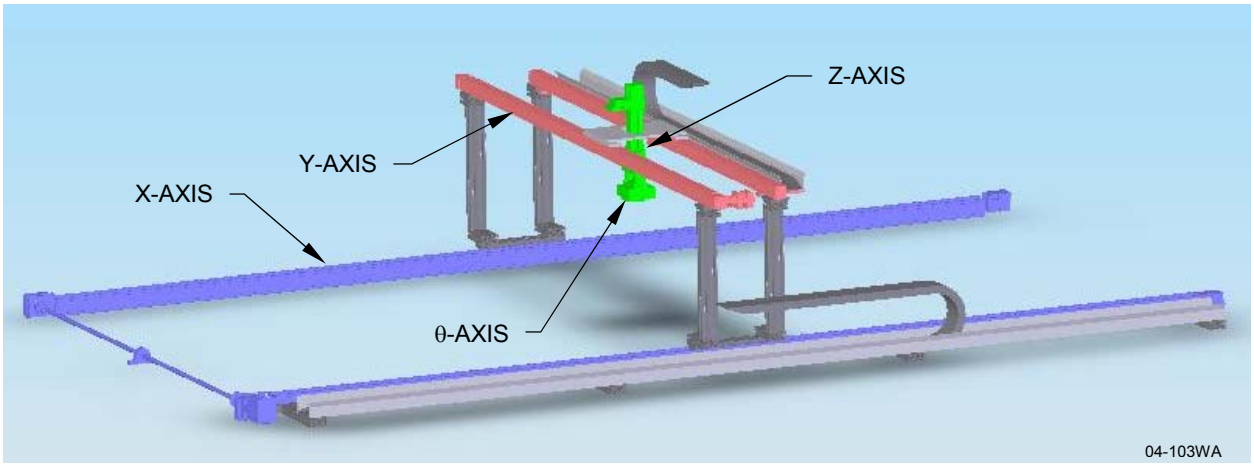

Figure 7 CAD model of four-axis Cartesian robot for busing assembly.

An end-effector was designed for the robot, including a safety clutch, a vacuum pick-and-place arm, and two soldering tips. The robot end-effector is shown in Figure 8. The clutch stops all robot motion in the event of a collision that applies torque on the end-effector. Each solder tip assembly includes a vertical air cylinder to move the solder tip below the vacuum cups during soldering, an air jet for rapid solder joint cooling, a heated spring-loaded solder tip, and a spring-loaded pin for holding the solder joint in contact while the solder freezes.

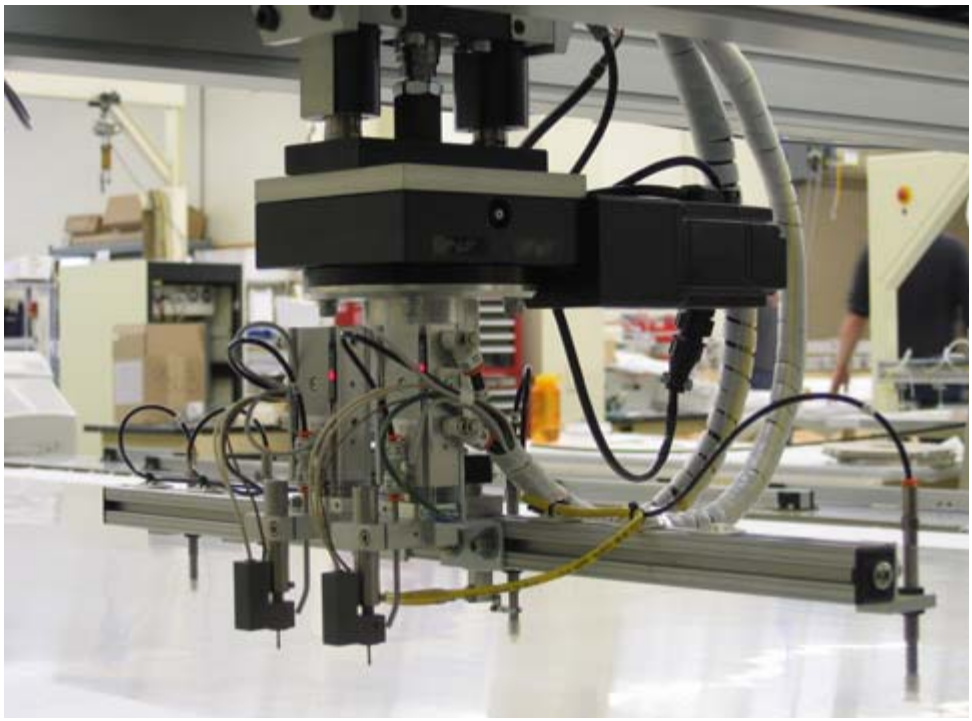

05-070WA

Figure 8 Robot end effector with soldering heads and vacuum pick-up arm.

Mechanical and electrical assembly of the bus and diode installation system was completed. The system is shown in Figure 9. A large 1.68 m x 6.10 m (66 inch x 240 inch) roller conveyor and a 4-axis Cartesian robot were installed on the main steel frame. A module stop assembly, two pneumatic module aligner assemblies, and three roller lift assemblies were built and installed on the conveyor for module alignment.

Tooling plates were installed on the frame on both sides of the conveyor. The two rear tooling plates hold the solder tip cleaner and three bus insulators for rear bus soldering. The robot places these reusable insulators under the bus ribbons to keep the EVA encapsulant from melting during soldering. The two front tooling plates hold three bus insulators for the front buses, seven bus ribbon trays (two short and two long trays for the front buses, and three trays for the rear buses), two diode pack retainers, and two flux applicator assemblies. A diode pack retainer, ribbon tray assembly, and flux applicator are shown in Figure 10. Each ribbon tray assembly has an optical sensor to signal when the tray is empty. The flux applicator has a float switch connected to a flux supply pump to maintain the proper flux level.

05-068WA

Figure 9 Module-size aluminum sheet on the automated busing system.

05-030WA

Figure 10 Bus ribbon tray (top), flux applicator (left), and diode pack retainer (center) on front tooling plate.

Electrical and pneumatics components were debugged. The digital and analog I/Os were verified, the robot actuators were configured, and the servomotors were tuned for the four robot axes (x, y, z, and θ). Software was written, installed, and debugged for the main operating screen (Figure 11), the I/O and motion diagnostics screens, the system parameters screen, and the process parameters screen.

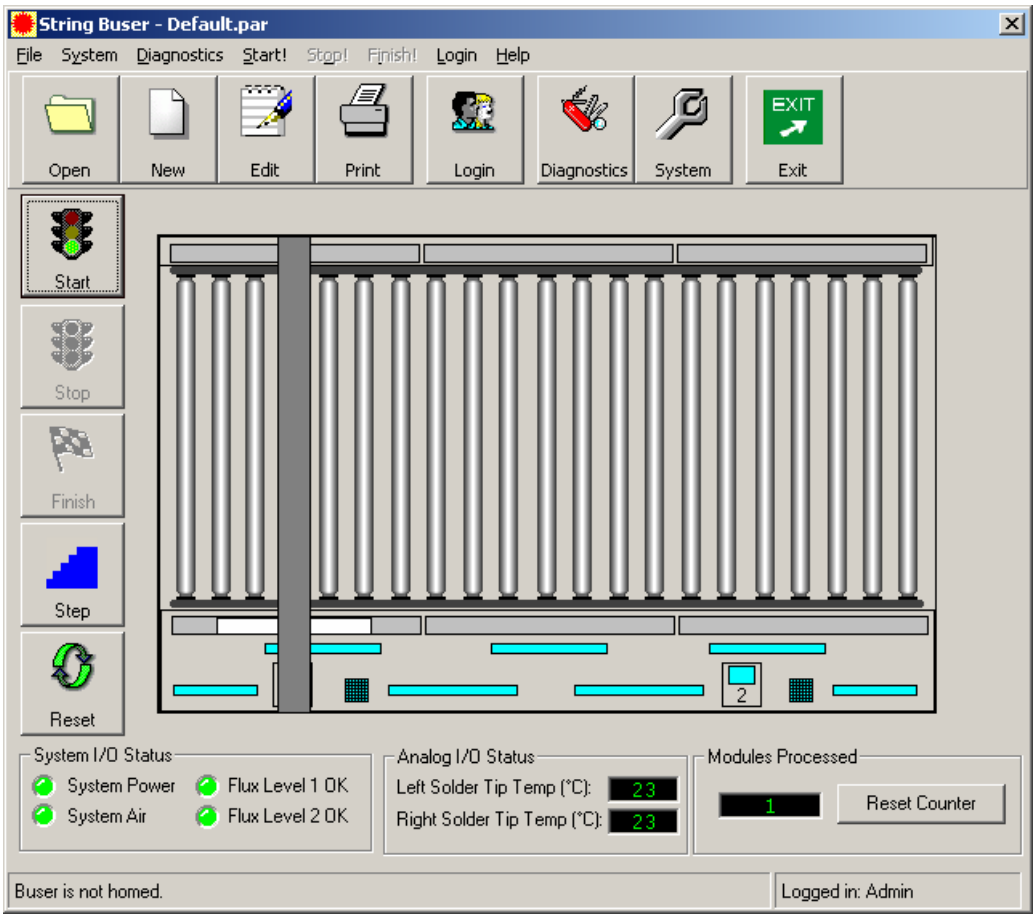

05-094WA

Figure 11 Main operating screen for the automated busing system.

Robot speed and position parameters were fine tuned for the bus ribbon and diode pick and place processes. Solder head motions were adjusted to eliminate ribbon bending when the soldering tips move down and contact the ribbon. Vertical (z axis) motions were minimized during the soldering moves to reduce process cycle time. A video of the busing system in operation was recorded and delivered to NREL.

2.2.3 Development Work at ARRI

ARRI designed and fabricated a prototype clamping mechanism to secure the bus bars in position during the soldering operation. The robot end effector acquires bus bars from a supply stack with vacuum cups, places them on the module, releases them, and retracts to allow placement of the soldering tips. A clamping mechanism was demonstrated that clamps the buses before the end effector releases the vacuum. The clamping devices are small and placed such that no interference occurs between the clamps and the soldering head. Once the joints are formed and solidified, the clamps are removed from the bus without disturbing the bus position on the module.

ARRI worked on developing and testing the bus-diode-bus soldering process with the Spire-designed solder head to establish ranges for soldering parameters, including reflow temperature, dwell time, tip pressure, and cool down period. The soldering parameters were initially refined using a manual process. Subsequent soldering tests were performed using an Adept 1 SCARA robot for automated processing.

In preparation for the solder tests, 610 mm lengths of 13 mm wide bus bars were cut, and one end of each strip was notched to match the diode area. Flux was applied in the robot-controlled process to the bottom surface of the diode and to the underside of the notched tab. The solder head temperature was maintained in the range from 264 °C to 278 °C. A reflow time of 8 s was used, followed by a cool down period of 2 s. The solder head assembly (shown in Figure 12) was mounted on a weighted slide that applied 2.4 kg of force to the joint during soldering.

05-004WA

Figure 12 Slide-mounted solder head suspended from robot arm.

Forty bus/diode/bus solder joints were formed and the joint strengths were measured using 90° pull tests (force applied perpendicular to the diode solder joints). All diodes were checked following soldering and prior to pull testing, and all tested good. Results from the 90° pull tests are plotted in Figure 13. The values are much more consistent than those observed with the manual soldering tests, implying that the previous variation was due to uneven contact or pressure between the solder tip and the materials to be joined. The majority of the strength values fall in the range of four to six pounds, and all are well above the target value of one pound. All joints are tested to complete failure. Once failure of the joint is initiated, complete failure occurs very quickly. It should be noted that, for all 40 joints, not one failed at the solder bonds between the diode and the buses. The consistent failure mode is through the center layer of the silicon diode.

ARRI designed and fabricated an experimental molybdenum solder head. The primary reason for modifying Spire's solder head design was to achieve better temperature control of the soldering tip, to determine whether the variations in solder joint strength observed in earlier tests were due to fluctuations in the tip temperature. Dimensions of the revised solder head are 0.75 inch by 0.75 inch by 1.94 inches. Two internal cylindrical cavities are machined to house a cartridge heater and a spring-loaded plunger pin assembly that holds the solder joint securely during the cool-down period. The solder head is shown in Figure 14.

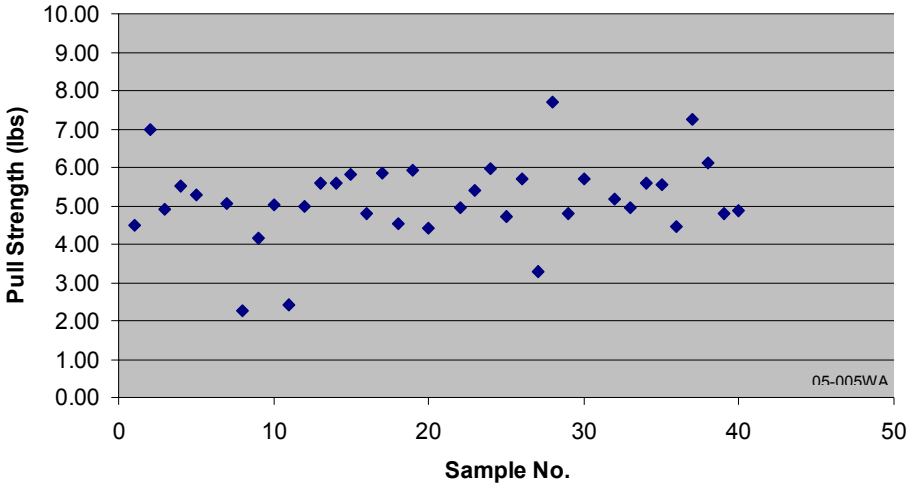

Figure 13 90° pull strengths of bus-diode-bus solder joints.

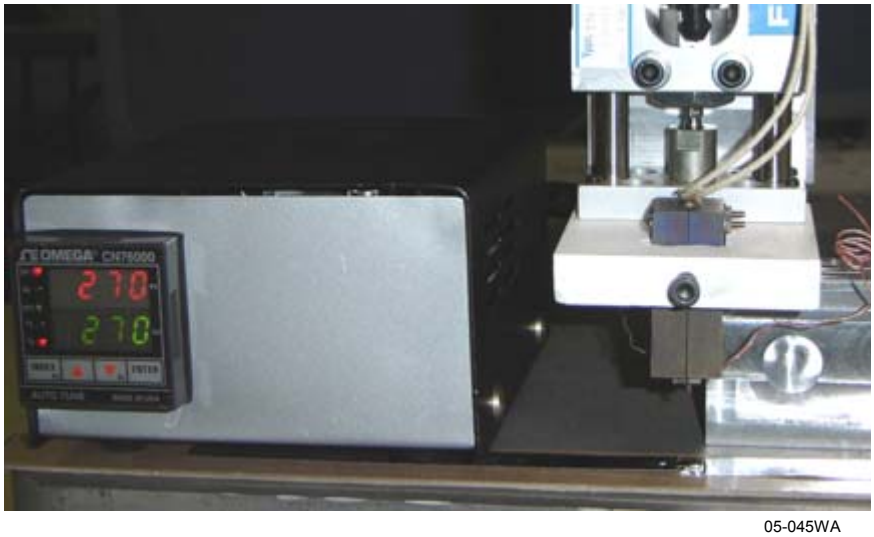

Figure 14 Experimental molybdenum solder head.

The solder head was connected to a PID temperature controller. During earlier soldering tests with the original solder head, the temperature of the soldering tip varied over a range of 14 °C, with the controller set at 270 °C. The temperature of the revised solder head was allowed to reach steady state, and then temperature measurements were taken just to the side of the soldering surface and recorded over a three minute time span. This was done for three temperature set points: 260 °C, 270 °C, and 280 °C. The temperature was very stable for all three settings. The greatest variation in temperature was 4 °C, observed at the 270 °C setting. Figure 15 plots the temperatures for the three settings over three-minute periods. Soldering experiments for the bus-diode-bus joint were performed using these three temperature settings. The process parameters are shown in Table 4.

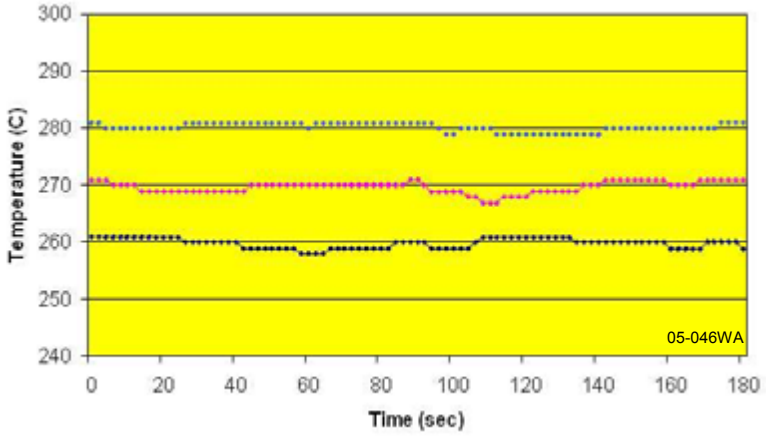

Figure 15 Temperature control of revised soldering tip with PID controller.

Table 4 Process parameters for soldering bus-diode-bus joints.

Reflow Temperature (°C)	Reflow Force (kg)	Reflow Period (s)	Cool-down Period (s)	Cool-down Force (kg)
260	2.4	8	5	0.23
270	2.4	5	5	0.23
280	2.4	5	5	0.23

Twenty solder joints were formed for each temperature setting, and then subjected to 90° pull tests to determine the joint strength and the failure mode. In 90% of the joints, failure occurred through the center of the diode, fracturing the bulk silicon. In the remaining 10% of the cases, the soldered interface between the diode and the bus bar failed. This type of failure had high strength, typically over 8 pounds. Pull strength data for joints made at 260 °C, 270 °C, and 280 °C are plotted in Figures 16 to 18. This data shows that, despite a more constant soldering tip temperature, the failure strength still varies. Based on this information, it was concluded that the moderate temperature fluctuations (±7 °C) of the original soldering head were not responsible for the variations in joint pull strengths. Since the lowest pull strengths occur when the silicon fractures, the variations may be due to stress in the diode caused by the difference in thermal expansion between the silicon diode and the copper bus bar.

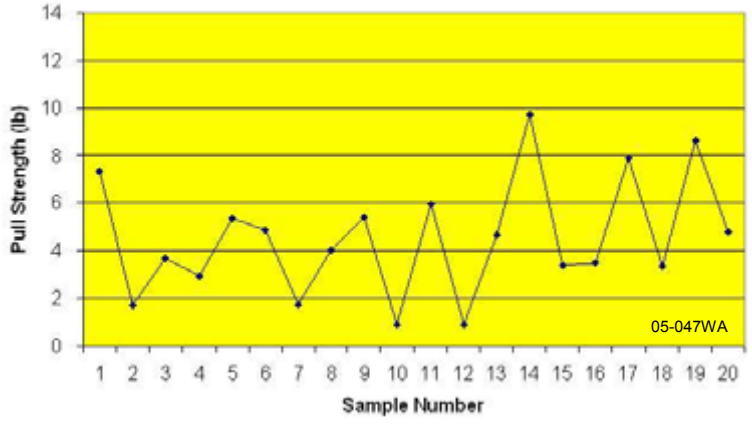

Figure 16 90° pull strength data for solder joints formed at 260°C.

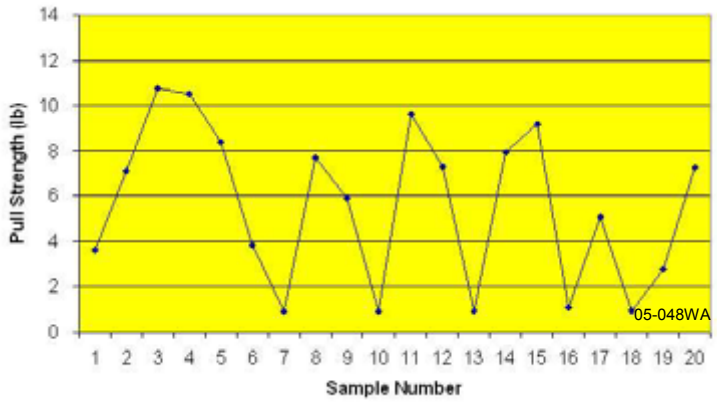

Figure 17 90° pull strength data for solder joints formed at 270°C.

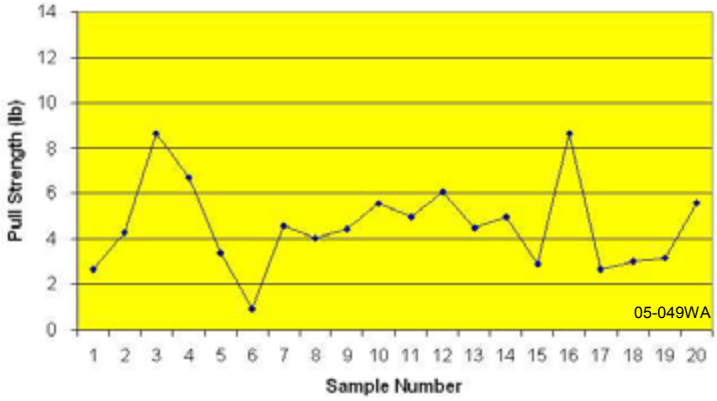

Figure 18 90° pull strength data for solder joints formed at 280°C.

Additional joints were soldered for the purpose of determining the shear strength of the bus-diode-bus joints. All joints were soldered at 270 °C using the parameters in Table 4. Pull tests were done with the force applied parallel to the diode solder joints. Joints that failed at the soldered interface had shear strengths ranging from 25 to 44 pounds. In other tests, the copper bus bar failed before the solder joint sheared, with shear strengths in the range of 42-54 pounds. A plot of the shear strength values is shown in Figure 19. This data shows that the shear strength of the bus-diode-bus joints far exceeds the level required for the module.

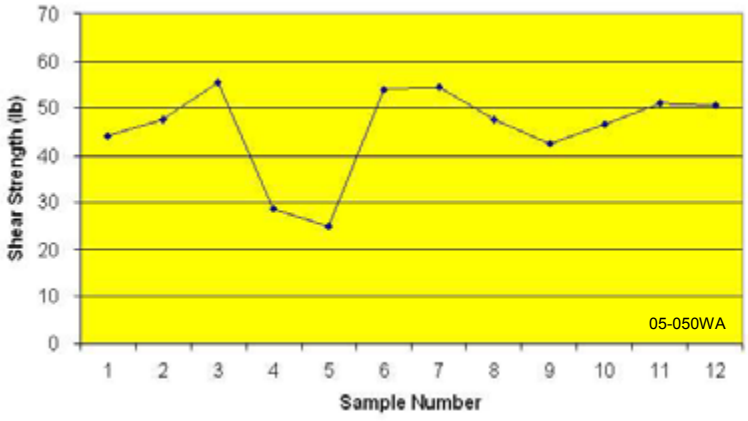

Figure 19 Shear strength for bus-diode-bus solder joints.

2.3 Task 8 – Design Advanced Lamination Process Tool

We designed an advanced laminator for large area PV modules in this task. Given the size of our module (1.57 m x 3.68 m), we decided to specify the lamination area at 2.00 m x 4.00 m. Initial design work focused on vacuum chamber structural design and heated platen design.

Solid models were created in CAD (SolidWorks) and a series of structural FEA simulations was done (with ANSYS) for various chamber plate thicknesses and reinforcing rib designs. Chamber deflection, stress, and factor of safety were calculated for each design. The load on the vacuum chamber is atmospheric pressure, set to 15 psi for these analyses. The resulting force on the chamber plates, which are 424 cm x 235 cm (167 inch x 92.5 inch), is 1,031 kN (231,700 lbf). Our design goals are to limit the total chamber deflection to 10 mm (0.39 inch) or less and to limit the stress on the chamber to obtain a factor of safety of 3 or more.

An early design iteration used 23 aluminum I-beams for reinforcing each of the two aluminum chamber plates. The chamber base has side walls around the perimeter to form the chamber cavity. The chamber cover design is similar to the base, except it has no side walls, which add stiffness to the base. The engineering simulation results are summarized as Case 1 in Table 5. The total maximum chamber deflection was 0.48 inch (base plus cover) under vacuum. The maximum stress was 18,000 psi, resulting in a safety factor of only 2.26. Thus both the deflection and the safety factor failed to meet our design goals in Case 1.

Table 5 Simulation results for large area laminator chamber deflection and stress under vacuum for three chamber designs.

Case	Chamber Component	I-beam Type	I-beam Quantity	Chamber Weight (lbs)	Maximum Deflection (inch)	Maximum Stress (psi)	Factor of Safety
1	Cover	4 x 4	23	2377	0.330	14,072	2.89
	Base	4 x 4	23	2633	0.150	17,998	2.26
	Total		46	5010	0.480		
2	Cover	8 x 5	19	2486	0.096	8,512	4.77
	Base	8 x 5	19	2742	0.057	5,377	7.55
	Total		38	5227	0.153		
3	Cover	8 x 5	13	2189	0.133	10,768	3.77
	Base	8 x 5	13	2445	0.080	7,702	5.27
	Total		26	4635	0.213		

We then switched to a taller, wider I-beam, and attached 19 of them, the most that would practically fit, to each plate. The total deflection decreased to 0.153 inch and the maximum stress decreased to 8,512 psi, for a safety factor of 4.77 (Case 2 in Table 5). Given that these results exceeded our structural design criteria by a wide margin, we reduced the number of I-beams to save cost and weight.

The final vacuum chamber design has 25 mm (1 inch) thick plates, each reinforced with 13 I-beams. The base chamber is shown in Figure 20, with a heating platen in place. The chamber deflects a total of 0.213 inch under vacuum (Case 3 in Table 5). The maximum stress is 10,768 psi, resulting in a 3.77 factor of safety. Results of the FEA simulations for cover deflection and stress for this design are shown in Figures 21 and 22.

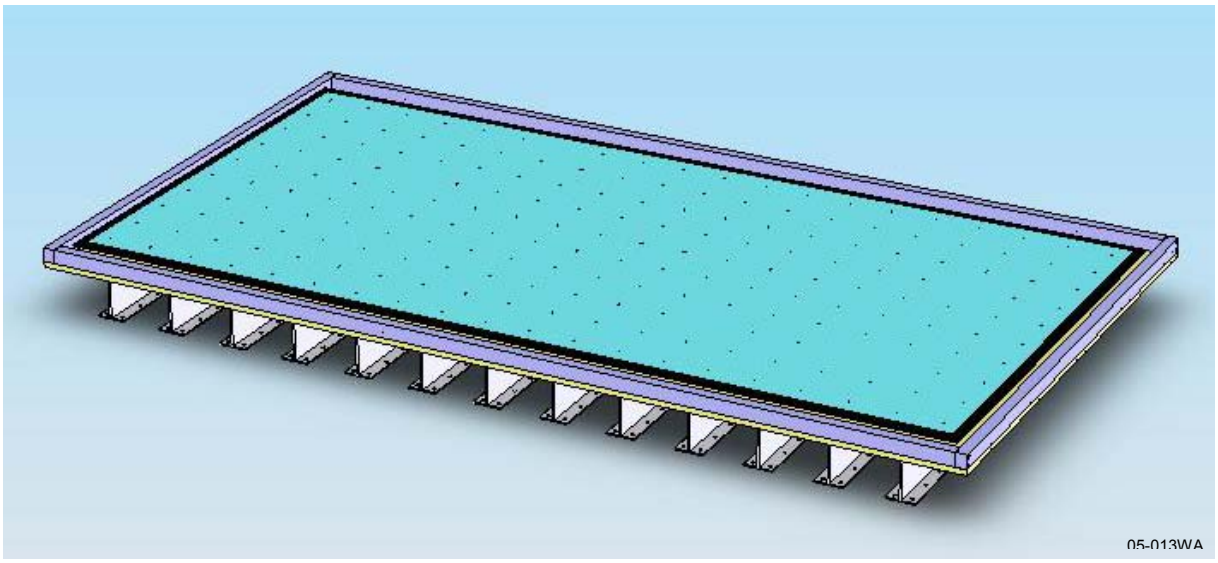

Figure 20 Vacuum chamber base design, 2 m x 4 m laminator (perspective view).

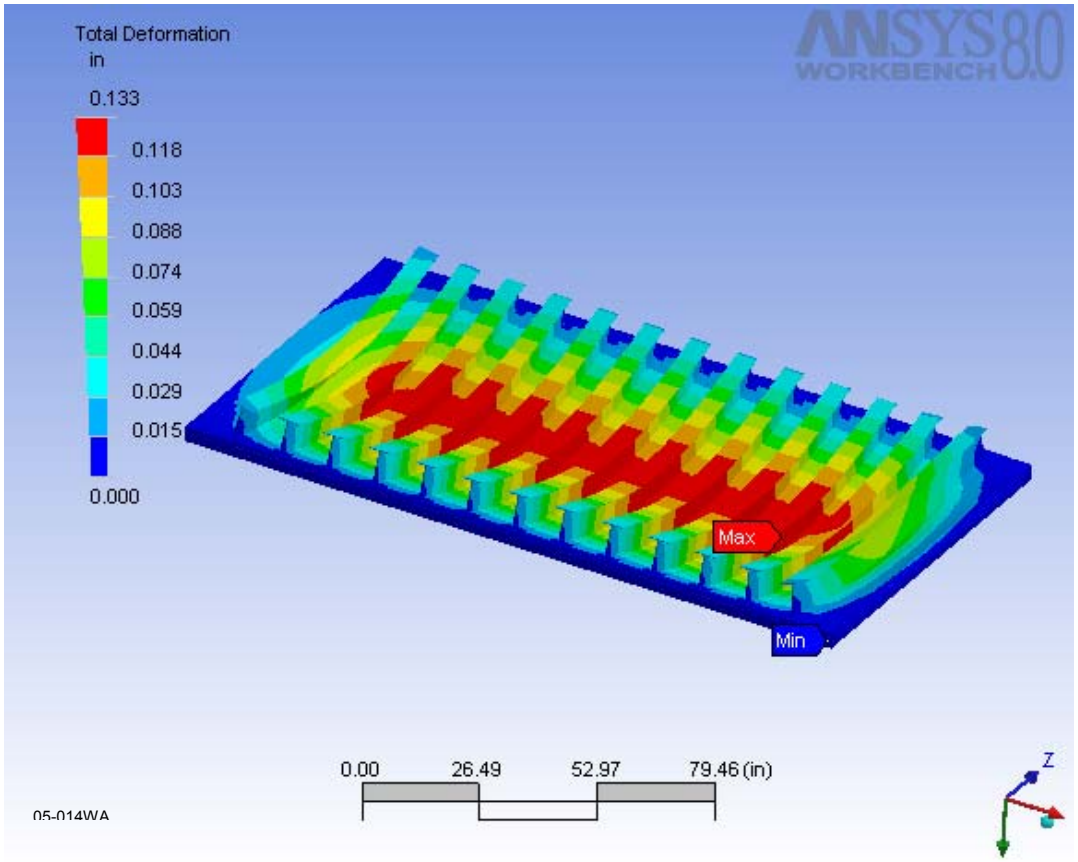

Figure 21 Chamber cover deflection under vacuum (inch).

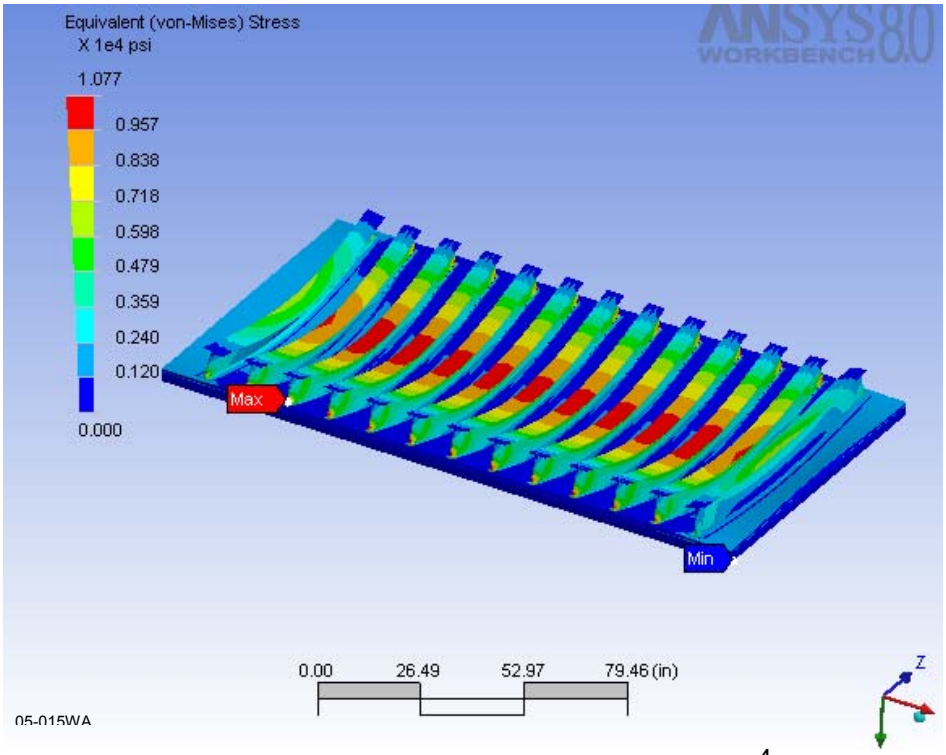

Figure 22 Chamber cover stress under vacuum (10^4 psi).

Once the chamber structural design was complete, design work focused on the remaining features of the vacuum chamber, the heated platen, and a module pin lift system. A perspective view of the complete vacuum chamber assembly design is shown in Figure 23. The chamber consists of top and bottom plates, side rails attached to the bottom plate to create the chamber cavity, and I-beams attached to both plates to limit the chamber deflection and stress under vacuum.

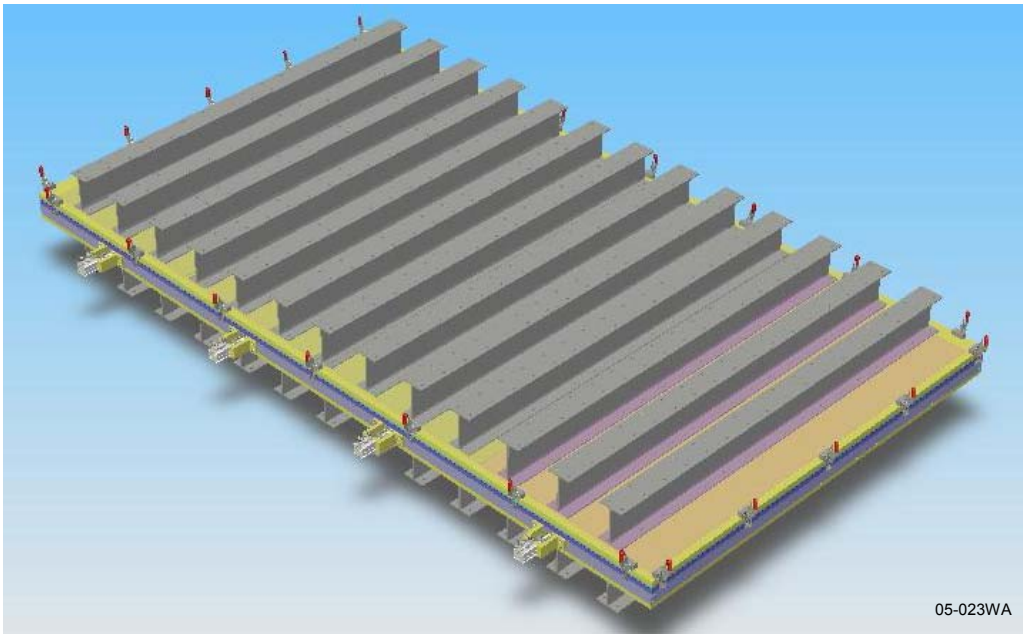

Figure 23 Large area laminator vacuum chamber design.

A quick-release diaphragm clamping system was designed that will significantly reduce the time required to change the flexible diaphragm that applies pressure to the module during lamination. The diaphragm clamp has an open rectangular shape, similar to a picture frame, which is attached to the bottom surface of the top chamber plate to hold the diaphragm in place. The new design uses a set of locking toggle clamps to hold the diaphragm clamp in place, instead of the large number of screws used in our previous designs. Figure 24 shows a cross-section view of the chamber assembly, while Figure 25 shows the overall laminator design.

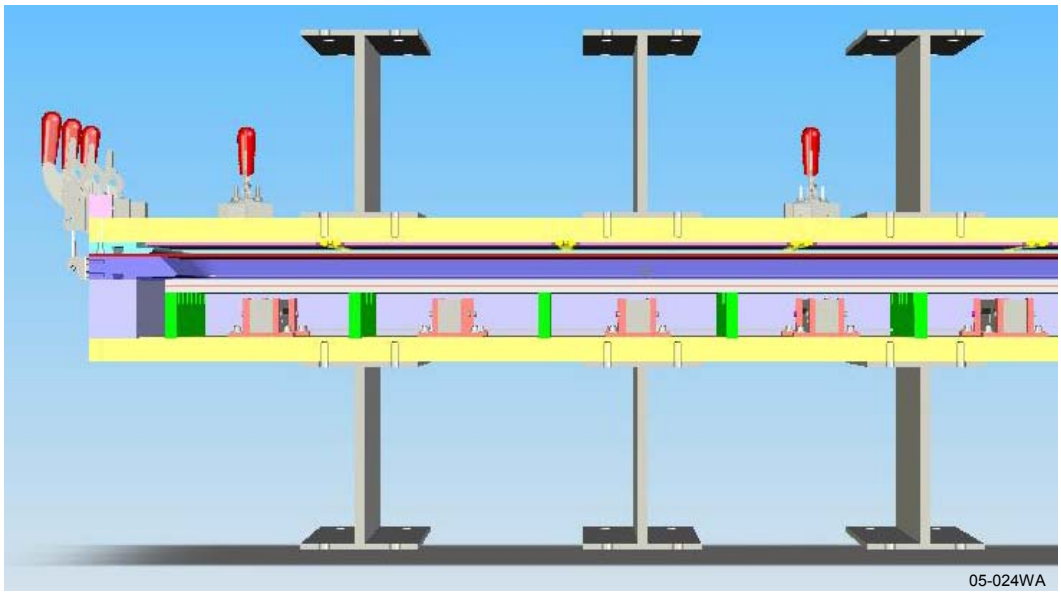

Figure 24 Laminator vacuum chamber design, cross-section view.

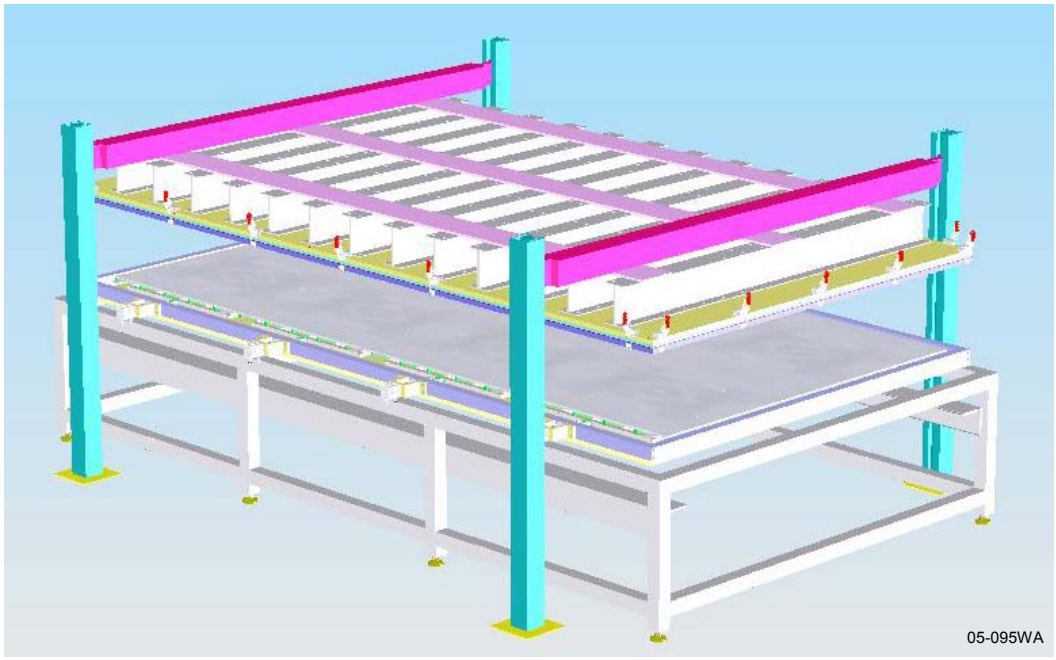

Figure 25 Large area laminator design model.

A module pin lift design was also completed for the large laminator. The pin lift is important to prevent large modules from curling when placed on a heated platen. Curling occurs because the surface of the glass in contact with the platen is hotter than the opposite surface of the glass, and therefore longer due to thermal expansion. The pins hold the glass slightly above the surface of the platen during the initial evacuation step in the lamination process. The pin lift system uses sliding cam bars under the heated platen to push pins, located in holes in the platen, from a position slightly below the surface of the platen up to a maximum height of 5 mm above the platen. The pin up height is adjustable, with a nominal 3 mm recommended for production.

We investigated the use of a novel blanket heater for the laminator's heated platen. Our current laminators use electric rod heaters attached to the platen with long machined clamps and thermal grease. Platen temperature uniformity is typically ±4 °C to ±5 °C. Improved uniformity can be obtained with rod heaters, either by making the platen thicker or by spacing the heaters closer together, which requires more heaters and clamps. Both options increase the cost of the laminator.

We identified a source of thin heaters that can be made in large areas, potentially at low cost. The flat geometry of these heaters may allow us to significantly improve the platen temperature uniformity. We obtained two 28 cm x 38 cm (11 inch x 15 inch) 230 V blanket heaters from the manufacturer for evaluations.

Our experience powering heaters in vacuum has shown that insulated power leads can produce conductive plasmas that arc to ground when operated at pressures in the 300 to 1000 mTorr range, which is the normal operating pressure in the laminator. These arcs can damage the insulation and the electrical controls while creating a potential safety hazard. Thus we designed and fabricated a simple vacuum chamber from two aluminum plates to test the blanket heater for potential arcing in vacuum. The chamber and heater controls were assembled and tested. A current sensor was installed on the heater power line and connected to an oscilloscope that would trigger if an arc occurs. The test setup is shown in Figure 26.

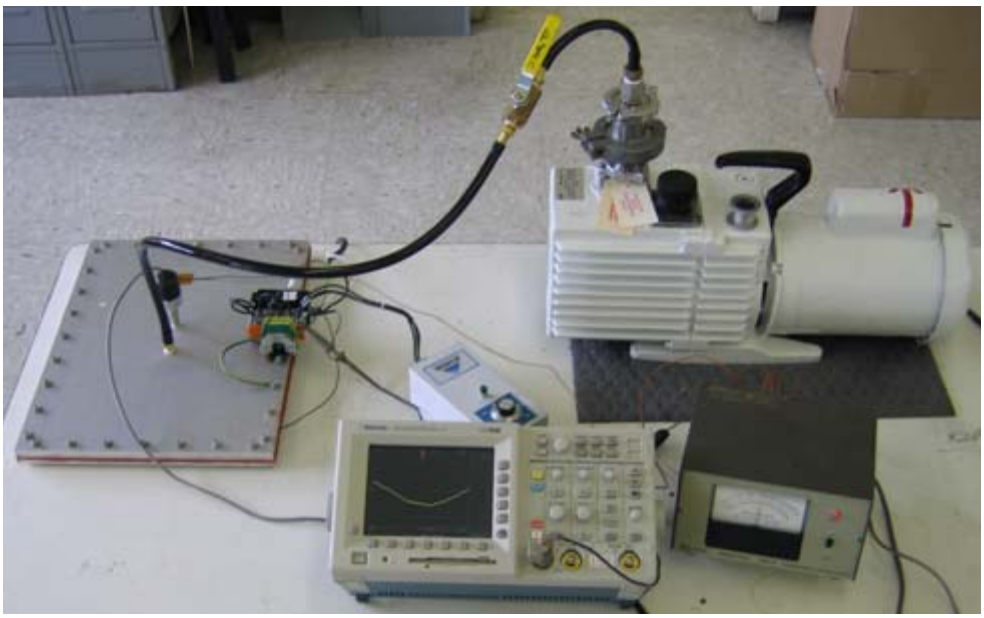

05-034WA

Figure 26 Blanket heater vacuum test setup.

Several scope triggers were detected, indicating possible arcing. We ran more tests to increase the chance that we would see the effects of arcing, then opened the chamber and examined the inside of the chamber and the heater. We found no direct evidence of arcing, such as carbon tracks or burned insulation. However, the heater insulation was delaminated internally from the heater element in some areas, probably due to overheating. We obtained information from the manufacturer on the temperature rating of the insulation used on the heater. We repeated this test with an identical heater, this time controlling the temperature below the rating for the insulation material. This time no arcs were detected.

Thermal cycling tests were completed for evaluating a graphite composite heat transfer material that may replace thermal grease in the laminator platen assembly. If the graphite material is suitable, it would eliminate the laminator maintenance and downtime that is sometimes required to replace grease that migrates away from the heater-platen interface due to thermal cycling.

The graphite material was installed around rod heaters and cooling lines in a test platen assembly and subjected to 2478 thermal cycles, typically between 100 °C and 160 °C. We then disassembled the platen and found that the graphite material was worn in some areas due to mechanical stress from thermal cycling. The graphite was removed and the test platen was reassembled with our standard thermal grease. Thermal cycles were then run while monitoring the platen temperature for comparison with the graphite data.

These tests showed that the temperature uniformity of our test platen is substantially better with thermal grease (±3.5 °C average) than with the graphite material (±6.7 °C average). This was a surprising result, given that the graphite material has a higher thermal conductivity (5 W/mK) than the thermal grease (0.95 W/mK). We suspect that the ability of the grease to flow and fill in gaps caused by irregularities in the mating surfaces is more important for uniform heat transfer than the difference in conductivity of the materials.

2.4 Task 9 – Design Lamination Automation

Mechanical design work was completed for an automated conveyor system for transporting modules through the large area laminator (2 m x 4 m module size capacity). The design is shown in Figure 27. The drive components for the conveyor were sized and selected. Mechanical design models for the drive conveyor and a conveyor cleaning brush were created. Detail design drawings and assembly drawings were generated from the models.

The conveyor belt will be fabricated from a Teflon®-coated fiberglass material, similar to the release sheets we use to keep EVA encapsulant from sticking to the interior surfaces of the laminator. A motor-driven cylindrical brush will be included to remove any EVA or other material that may accumulate on the belt.

A view from the CAD model of the conveyor drive design is shown in Figure 28. The laminator vacuum chamber will sit inside the drive system, with the heated platen and chamber side walls coplanar with the conveyor belt. Belt travel is left to right in Figure 28.

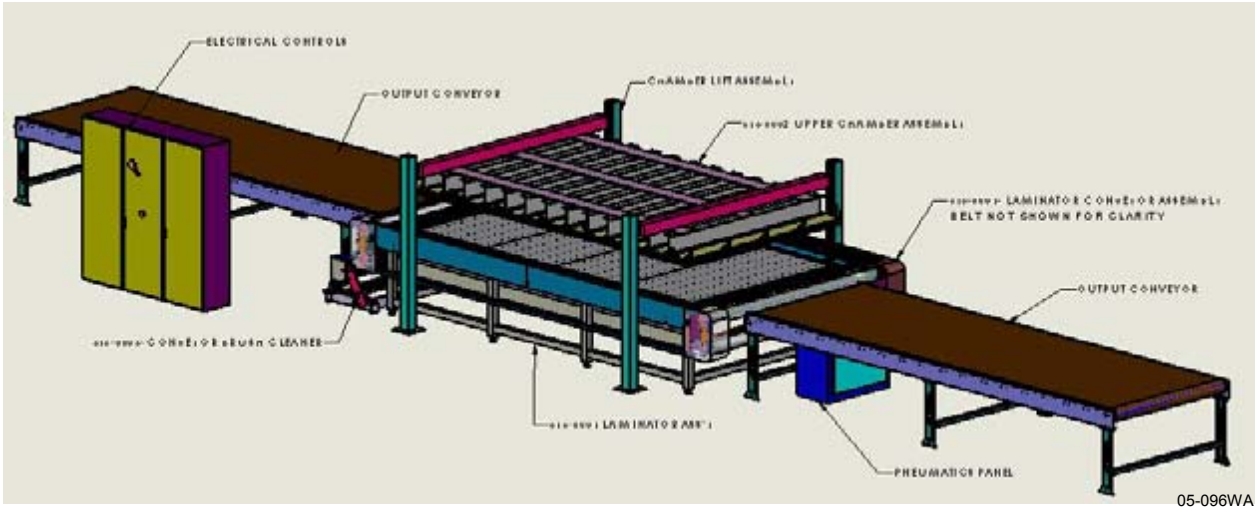

Figure 27 Laminator automation design.

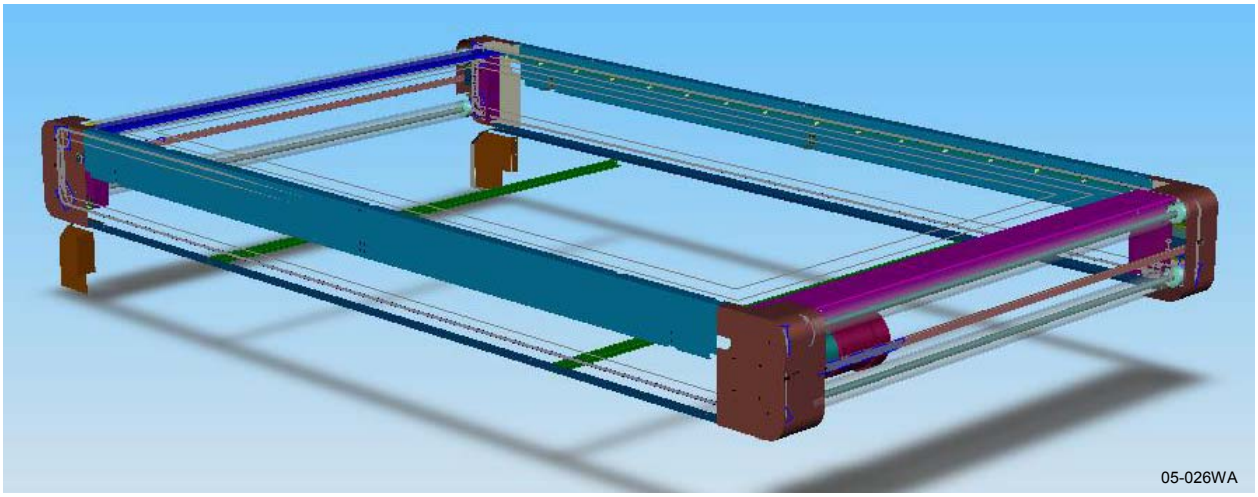

Figure 28 Module conveyor drive design for laminator automation (conveyor belt not shown for clarity).

2.5 Task 10 – Design Large Area Solar Simulator

Spire currently produces upward flashing solar simulators that can test modules up to 1.37 m x 2.00 m. In Task 10 we designed a simulator with a significantly larger 2.0 m x 4.0 m test area for the Brightfield module. We maintained the flash up geometry for the larger simulator, since it simplifies product handling by allowing modules to be transported over the simulator on a conveyor.

A view of the solid CAD model of the simulator is shown in Figure 29. The simulator has four 2.0 m long xenon lamps positioned side-by-side under the test plane. Adjustable reflecting surfaces direct light to the test plane, while optical filters correct the spectrum to Air Mass 1.5 Global, per ASTM E 927-04[2]. A pair of motor-driven belt conveyors supports the module at its edges and transports it through the simulator. The conveyor positions are adjustable to suit the module width.

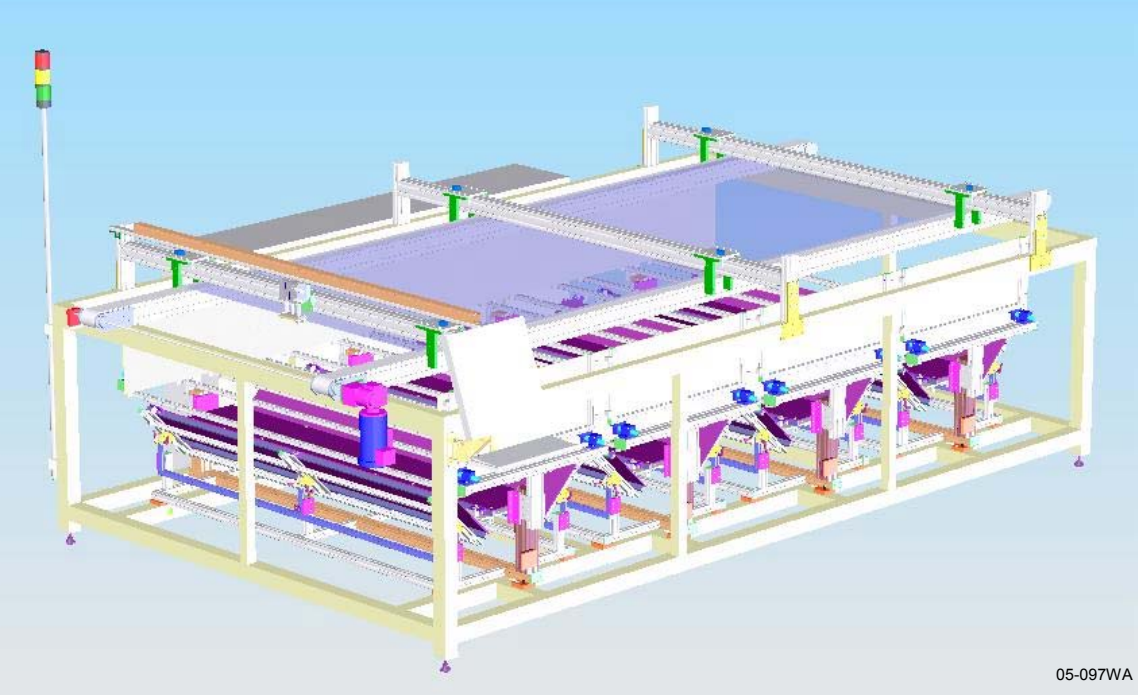

Figure 29 Large area solar simulator design with 2 m x 4 m test plane. Side panels removed for clarity.

2.5.1 Single-Flash Long Pulse Xenon Light Source

We developed a single-flash, long pulse xenon light source for our solar simulator. Our standard simulator uses multiple (50 to 200) short pulses (1 ms per pulse at 7 to 10 Hz) for each module I-V curve. A single flash approach, in which an I-V curve is measured in a single lamp flash, shortens the test time from ~20 s to less than 1 s per module. A longer pulse, on the order of 100 ms, allows the simulator to be used for solar cells with slow response times, such as SunPower Corporation's high efficiency (20%) back contact cells and Sanyo's Heterojunction with Intrinsic Thin Layer (HIT) cells.

We successfully developed a unique active feedback lamp control system that uses power semiconductors (MOSFETs) to control the flash profile of a xenon lamp. This lamp control method allows us to build a long pulse, single flash simulator without a large number of big, heavy, and expensive inductors.

We designed, assembled, and tested a prototype lamp regulator printed circuit board (Spire no. 909-0401), shown in Figure 30. The board controls the gate drive of a bank of high voltage power MOSFETs in response to an applied reference signal. Initial checkout involved applying signals to the board from a function generator and observing the behavior of the board. Changes were made to some board components as a result of these tests.

Work then began on discharging a large (2400 μF, 3600 VDC) capacitor with a regulated current, in preparation for a controlled flash of a xenon arc lamp. An electrical panel was assembled, including the Spire lamp regulator board, four power MOSFETs, and several high voltage relays and power resistors, which provide backup discharge capability.

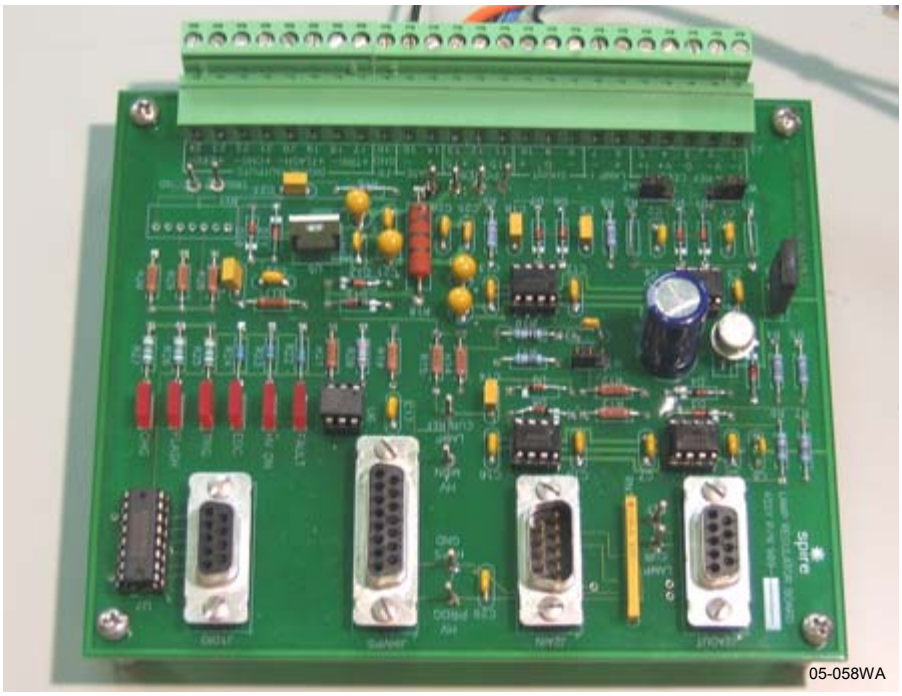

Figure 30 Spire lamp regulator circuit board for a single-flash long-pulse solar simulator.

The capacitor was first discharged through a 180 Ω power resistor network. This was successful up to the point where MOSFET failures occurred, due to transient over-voltage during turn-on. We then substituted a 1955 mm long xenon arc lamp in place of the resistor network, since its terminal voltage is effectively independent of current. The lamp flashed successfully at a constant current set point of 6.3 A. Two additional MOSFETs were installed on the panel, and lamp current was increased in steps up to 16 A, at an operating voltage of 2350 V. The pulse width under these conditions was about 65 milliseconds at constant current.

A reference cell was then installed and used as the feedback source for the light pulse, which is our ultimate lamp control scheme. This circuit produced flashes with very uniform light intensity for 66 ms. The light pulse has an initial spike followed by a long flat region, which ends when the capacitor is discharged to the point where it can no longer provide sufficient current to the lamp. The pulse length was then increased by adding more capacitance to the circuit. Figure 31 shows a 78 ms flat light pulse generated by a 1.955 m long xenon lamp with 3600 μF capacitance. The lamp current was 24 A during the flash, sufficient to produce 1 sun (100 mW/cm^2) of light intensity in a solar simulator.

The controlled flash has much better intensity stability than obtained with a traditional passive pulse-forming network composed of capacitors and inductors. Initial tests show the temporal instability of irradiance is less than 0.1%, which is an order of magnitude better than that obtained with a passive network, and well below the 2% Class A specification in ASTM E 927-04[2]. Additionally, active control provides excellent flash-to-flash repeatability. As a consequence, more accurate I-V data can be obtained.

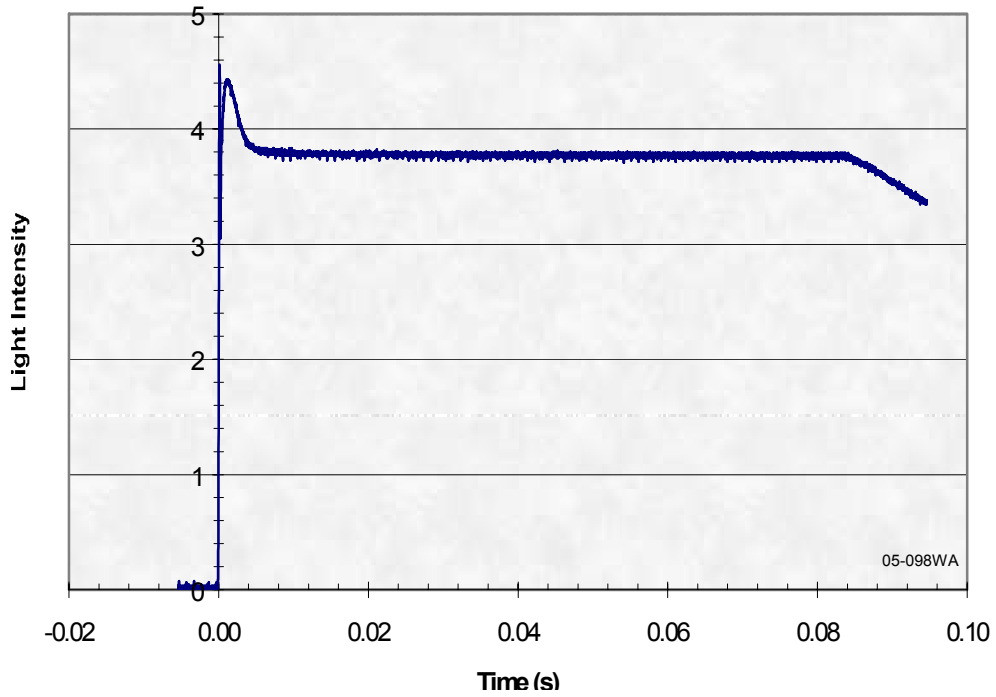

Figure 31 Scope trace of light intensity during a xenon lamp flash using an active lamp control circuit. The flat portion of the pulse is 78 ms long.

2.5.2 Large Area Optical Test Bed

We investigated methods for improving the light spatial uniformity of the large area solar simulator. Our current simulators are able to achieve ±3% uniformity over the test plane, which is remarkable given the short lamp to test plane distance (less than one meter). A considerable amount of effort goes into the uniformity tuning process for each simulator, to meet the ±3% specification. An alternative optics design is being evaluated that may allow us to improve our uniformity with less tuning. Another benefit of this design is that it reduces the area of spectral filters, which will save considerable cost.

A two-lamp optical test bed assembly was designed and built (Figure 32) to test the feasibility of the new optics over a 2 m x 2 m test plane. An electrical control box was completed and installed near the test bed. Two lamp trigger boards were assembled and installed on the test bed.

Reflector assemblies were fabricated by attaching 76 μm (0.003 inch) thick reflector film onto flat substrates. The substrates were spray coated with a contact adhesive and the reflector film was rolled onto the substrate with a roller laminator, which has motor driven pinch rollers with pneumatic pressure control. Unfortunately, the resulting reflector surface had an orange peel texture, due to the thinness of the reflector film and the unevenness of the spray coated adhesive. Since this texture might reduce the spatial uniformity of the light at the test plane, we replaced the thin reflector film with 760 μm (0.030 inch) thick reflector sheets. The sheets were cut to size and attached to the substrates with contact adhesive. The resulting reflector surfaces are smooth. The reflector assemblies were installed on the test bed.

Figure 32 Solar simulator optical test bed with 2 m x 2 m test area.

The two lamp assemblies will illuminate a 2 m x 2 m test plane. Normally, a reference cell is placed on the test plane and moved in a grid pattern to measure the spatial uniformity of the light intensity. However, our 2 m x 2 m test bed has no physical test plane on which to rest a reference cell. (The 2 m x 4 m sun simulator will also have no physical test plane, as we plan to transport modules across the simulator supported by a pair of narrow belt conveyors at the module edges.) Thus we designed and built a gantry, shown in Figure 33, that suspends a monitor cell at a fixed height over the test bed. The monitor cell is mounted on a small carriage that is moved incrementally in x and y directions as the lamps are flashed to map the simulator spatial uniformity.

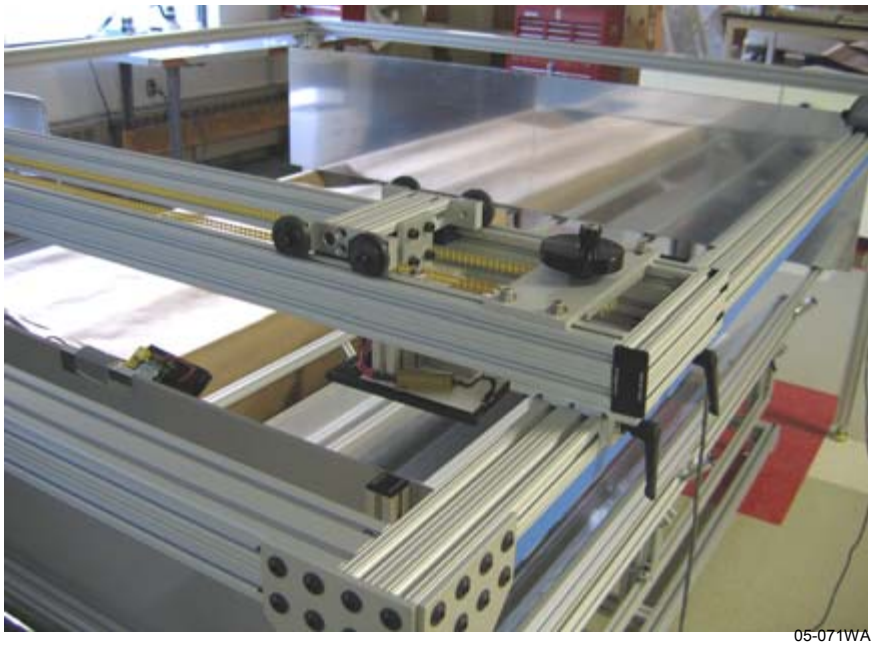

Figure 33 Monitor cell gantry for measuring light uniformity over a 2 m x 2 m test area.

2.5.3 High Power Electronic Load

We are increasing the power capacity of our electronic load and measurement circuitry, which measures module I-V curves. Our Brightfield module will produce 811 W at Standard Test Conditions (100 mW/cm^2, 25 °C) when fabricated with 15% efficient solar cells. Since this is well beyond the 500 W rating of our current electronic load circuit board, we are redesigning it to handle module power levels up to 1000 W when illuminated by a long pulse single flash solar simulator.

Commercial bipolar power supplies were rejected due to cost ($6500 unit price), size (19-inch rack mount) and weight (24 kg). A passive capacitor type system was considered but rejected, due to the potential difficulty of matching appropriate module characteristics with varying pulse lengths. An active current control system composed of parallel power MOSFETs was ultimately selected, as the I-V sweep can be controlled precisely.

The circuit will operate by sweeping device current from I_{sc} to V_{oc}. A power MOSFET was selected for this purpose due to its optimization for linear use and its voltage and current ratings. Depending on the selected range, current is diverted through one or two shunt resistors and the resultant signal is fed to a programmable gain amplifier. This arrangement allows four current ranges to be selected by two control signals. The device voltage, after passing through an attenuator (approximately 25:1), is amplified by two successive stages. The first features selectable gains of 1, 2.5, and 10; the second features gains of 1 and 10. In this way, five voltage ranges (gains of 1, 2.5, 10, 25, and 100) can be obtained using three control signals. An on-board capacitor bank will compensate for voltage drops in the semiconductors and shunt resistors. The capacitors will be pre-charged through a relay and then isolated prior to measurement.

2.6 Task 11 – Develop Soldering Process for Thin Cells

Our objective in this task is to develop a high-yield soldering process for joining thick copper interconnect ribbon to thin silicon solar cells. As cells become larger and more efficient, the amount of current they produce increases. If the interconnect ribbon cross-section remains constant, power loss in the ribbon increases as I^2R. Therefore, it would be beneficial to increase the ribbon thickness to reduce its series resistance without increasing its width, since the width shadows the cell. However, the stress on a cell's solder joints increases with the thickness of the copper, so there is a limit where the copper thickness begins to cause fracturing of the silicon. This limit is typically 125 μm (0.005") for soft annealed copper. The problem is worse for thin cells, less than 250 μm thick, which fracture more easily than thicker cells. In this task we developed a method of forming shallow fine-pitch corrugations in copper ribbon that act as stress-relief features to enable the use of thicker ribbon.

We ran a test with thin cells to evaluate cell stress cracking with thick flat ribbon. Cell strings were fabricated from thin 220 μm cells and thick 178 μm (0.007 inch) ribbon on our automated solar cell stringing equipment, the Spi-Assembler™ 5000. When flexed after soldering, the thin cells consistently break at the same spot, where the maximum stress occurs, as shown in Figure 34. The location is the end of the solder joint on the back of the cell.

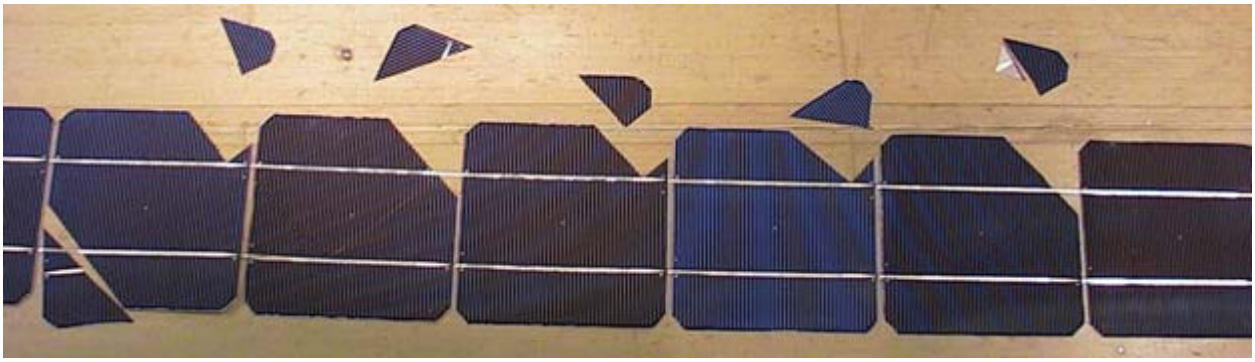

05-099WA

Figure 34 String of 220 μm cells soldered with 178 μm thick flat copper ribbon and flexed to show crack locations.

A ribbon spool drive assembly with corrugators was designed to integrate the ribbon corrugation function into our Spi-Assembler 5000. The assembly includes support rollers for two ribbon spools and two motor-driven corrugator assemblies. Components were fabricated, assembled, and tested with thick copper ribbon at Spire in Bedford, MA. The assembly was then shipped to our Chicago module fabrication facility, where it was installed on an Assembler. Solar cell strings made with thin cells and thick corrugated interconnect ribbons were produced with this equipment. The type of consistent cracking seen previously with flat ribbon was not evident in these strings. Two of these strings are shown in Figure 35.

05-072WA

Figure 35 Cell strings made with 220 μm thin cells and 178 μm thick corrugated interconnect ribbons.

Each string consists of four cells soldered in series. We used 220 μm thick x 125 mm square Cz-Si cells from Shell Solar and 178 μm (0.007 inch) thick x 2.0 mm (0.080 inch) wide copper ribbon with 13 to 18 μm (500 to 700 micro-inch) thick Sn62/Pb36/Ag2 solder coating.

While we were able to produce good strings, these tests showed the need for some improvements to the corrugator assembly. The drive motors had trouble pulling the ribbon from the heavy (5 kg) spools, a problem that will be solved by using higher torque motors. The corrugated ribbon had variable camber (bow in the plane of the ribbon) because the spools are wide (101 mm between flanges), resulting in a

large variable angle as the ribbon feeds into the corrugator. This will be corrected by increasing the ribbon path length between the spools and the corrugators. Design work for the larger motor and the longer ribbon path was completed and is shown in Figure 36.

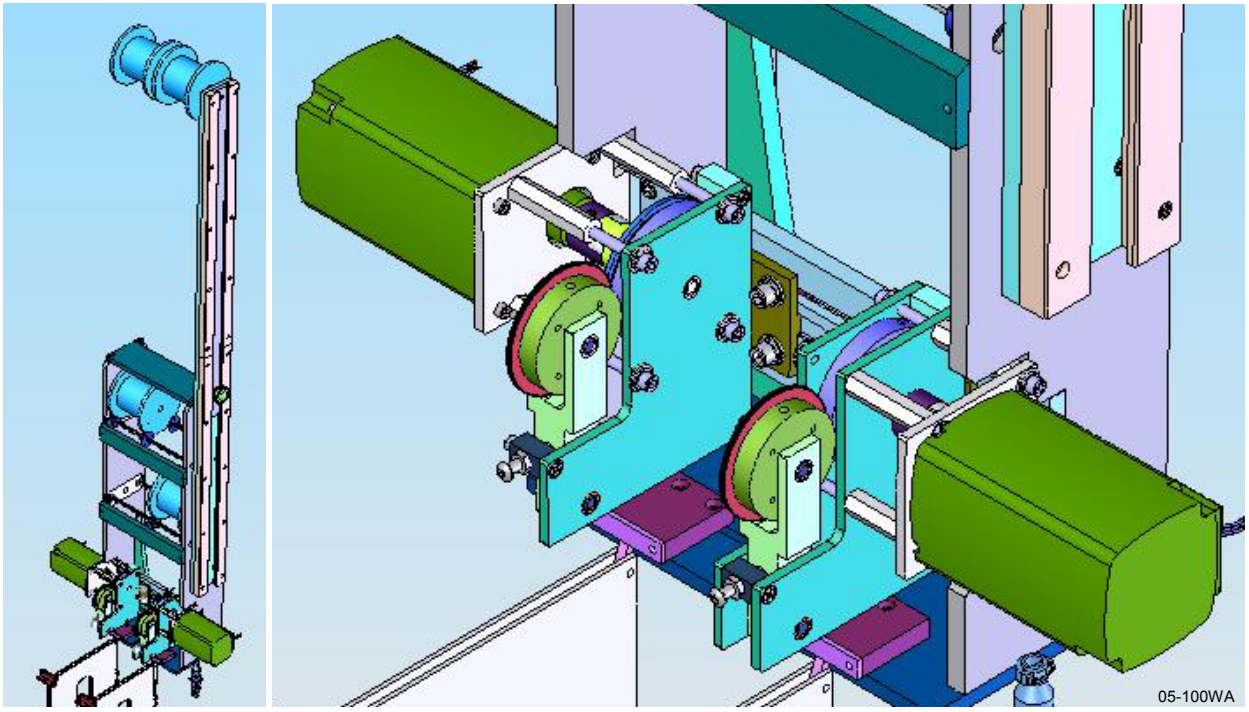

Figure 36 Ribbon spool drive assembly with corrugators (left) and close-up of the ribbon corrugator assemblies (right).

3 CONCLUSIONS

Spire has completed the second phase of a three-phase program for developing automated production line processes for solar Brightfield modules. In the first phase, a large area (1.57 m x 3.68 m) 800 W module for utility-scale PV arrays was designed, with emphasis on minimizing Balance of System (BOS) costs. Unique module features include internally laminated by-pass diodes, which greatly simplifies the module's internal busing and output terminals, and a cantilevered superstrate that allows for a reduced glass thickness and a simpler frame design. Another key Phase 1 accomplishment was the development of a cell string inspection system with machine vision and microcrack detection capabilities. Spire applied for a U.S. patent on the infrared crack detection technique.[3]

In Phase 2 we worked on the design and development of automated tools for producing such modules in multi-megawatt per year quantities. Major achievements include:

- An automated system for dispensing and laying up module materials (encapsulant and back sheet) was fabricated and tested. The system feeds material, cuts it to length, and places it in position directly on the module. An in-line punch cuts a narrow rectangular hole along one edge of the sheet for feeding bus leads through to the module output boxes. Testing was done to measure the accuracy of cut lengths, hole locations, and sheet placement on the module for stable and elastomeric sheets.
- We fabricated and tested an automated system for installing and soldering bus ribbons and diodes in modules prior to lamination. The system comprises two machines, a bus ribbon fabrication machine and a bus and diode installation machine.
    - The bus ribbon fabrication machine automatically feeds ribbon from reels, straightens it to remove coil set, cuts or punches it to length, and fills a tray with a stack of ribbon. The punch trims one end of the bus to match the diode width, to prevent the positive and negative buses from shorting out the diode.
    - The bus and diode installation system consists of a conveyor and aligner for 1.6 m x 3.7 m modules and a 4-axis robot with a custom end-effector for placing bus ribbon, applying flux, placing diodes, and soldering bus ribbons. The robot also places reusable insulator strips on the module to prevent the encapsulant from melting during the soldering process. Spire's constant temperature hot-bar solder tip was used for soldering the cell string ribbons and the diodes to the bus ribbons. Solder joint pull strengths far exceeded the 450 g target value when pulled at a 90° angle and in shear.
- We designed an advanced vacuum laminator for large PV modules. The lamination area (2.0 m x 4.0 m) is more than twice the size of our current largest model. Vacuum chamber structural design work was done using finite element analysis to optimize the chamber structure while maintaining deflection and stress within acceptable limits. A new heated platen design was conceived in which a blanket heater is used in place of rod heaters for improved temperature uniformity. A module pin lift design was incorporated to prevent glass bowing during the initial pump-out phase of the lamination cycle. A quick-release diaphragm clamp system was designed to reduce equipment downtime during diaphragm replacement. A vertical cover lift was designed to reduce the time needed for loading and unloading modules.
- Mechanical design work was completed for an automated conveyor system for transporting modules through the large area laminator (2 m x 4 m module size capacity). The drive components for the conveyor were sized and selected. Mechanical design models, assembly drawings, and detail drawings were created for the drive conveyor and a motor-driven conveyor cleaning brush assembly.

- We designed a solar simulator with a 2.0 m x 4.0 m large test area for measuring the electrical performance of the Brightfield module under simulated sunlight. This test area is nearly three times the size of our current largest simulator. We used a flash-up geometry to simplify product handling by allowing modules to be transported over the simulator on a conveyor. The simulator has four 2 m long xenon lamps positioned side-by-side under the test plane. Adjustable reflecting surfaces direct light to the test plane, while optical filters correct the spectrum to Air Mass 1.5 Global, per ASTM E 927-04[2].
    - We developed a single-flash, long pulse xenon light source for the solar simulator, in place of our standard multiple-flash short-pulse xenon lamp. The single flash shortens the measurement time from ~20 s to less than 1 s per module. The long pulse increases the illumination time up to 100 ms, compared to our standard 1 ms pulse, to allow the simulator to measure the performance of high efficiency and thin film modules with slow response.
    - A unique active lamp control scheme was devised for the long pulse lamp. Lamp intensity is controlled by active feedback from a reference cell. Extremely flat, well-controlled pulses up to 78 ms were demonstrated. Tests showed the temporal instability of irradiance is less than 0.1%, which is an order of magnitude better than that obtained with a passive network. The pulse length can be increased to 100 ms or beyond simply by increasing the capacitance of the lamp circuit.
- We demonstrated a method for forming shallow, fine-pitch features in thick copper ribbon to reduce stress and maintain high yield in the cell string soldering process. We designed an automated ribbon forming assembly that was incorporated into our automated cell string assembly equipment. This equipment successfully assembled cell strings made with 220 μm thick Cz-Si cells and 178 μm thick copper ribbon. This technology can be applied to reduce the breakage rate of thin cells in the string soldering process, and to allow the use of thicker copper ribbon to reduce module power loss due to ribbon series resistance. Spire has filed a provisional application for a US patent for this technique.[4]

In the remaining third phase of our program, we plan to fabricate and test the improved large area laminator, the module transport automation for the laminator, and the large area sun simulator. We will also develop a computer integrated manufacturing system for module line supervisory control and data acquisition.

4 REFERENCES

1 Tedlar® is a registered trademark of DuPont for its polyvinyl fluoride (PVF) film.

2 ASTM E 927-04, "Standard Specification for Solar Simulation for Photovoltaic Testing," ASTM International, West Conshohocken, PA, 2004.

3 U.S. Patent Application No. 10/709,529, "Infrared Detection of Solar Cell Defects Under Forward Bias," filed May 12, 2004.

4 Provisional US Patent Application, "Corrugated Ribbon and Process for Low-stress Soldering of Leads to Solar Cells," submitted November 2005.

REPORT DOCUMENTATION PAGE

Form Approved
OMB No. 0704-0188

PLEASE DO NOT RETURN YOUR FORM TO THE ABOVE ORGANIZATION.

1. REPORT DATE *(DD-MM-YYYY)*	2. REPORT TYPE	3. DATES COVERED *(From - To)*
August 2006	Subcontract Report	1 July 2004–15 October 2005

4. TITLE AND SUBTITLE
Development of Automated Production Line Processes for Solar Brightfield Modules: Final Annual Technical Progress Report, 1 July 2004 – 15 October 2005

5a. CONTRACT NUMBER
DE-AC36-99-GO10337

5b. GRANT NUMBER

5c. PROGRAM ELEMENT NUMBER

6. AUTHOR(S)
M.J. Nowlan, J.M. Murach, S.F. Sutherland, D.C. Miller, S.B. Moore, and S.J. Hogan

5d. PROJECT NUMBER
NREL/SR-520-40406

5e. TASK NUMBER
PVB66101

5f. WORK UNIT NUMBER

7. PERFORMING ORGANIZATION NAME(S) AND ADDRESS(ES)
Spire Corporation
One Patriots Park
Bedford, Massachusetts 01730-2396

8. PERFORMING ORGANIZATION REPORT NUMBER
ZDO-3-30628-12

9. SPONSORING/MONITORING AGENCY NAME(S) AND ADDRESS(ES)
National Renewable Energy Laboratory
1617 Cole Blvd.
Golden, CO 80401-3393

10. SPONSOR/MONITOR'S ACRONYM(S)
NREL

11. SPONSORING/MONITORING AGENCY REPORT NUMBER
NREL/SR-520-40406

12. DISTRIBUTION AVAILABILITY STATEMENT
National Technical Information Service
U.S. Department of Commerce
5285 Port Royal Road
Springfield, VA 22161

13. SUPPLEMENTARY NOTES
NREL Technical Monitor: Brian Keyes

14. ABSTRACT *(Maximum 200 Words)*

Spire Corporation is addressing the Photovoltaic Manufacturing R&D project goals of improving photovoltaic (PV) manufacturing processes and products while reducing costs and providing a technology foundation that supports significant manufacturing scale-up. To accomplish this, we are focusing our efforts on the design of a large-area utility-scale module and the development of the necessary manufacturing techniques and equipment to manufacture such a module in a high-volume production environment. A three-phase program is under way for developing and demonstrating new automated systems for fabricating very large PV modules ideal for use in multi-megawatt grid-connected applications. We designed a large-area (1.57 m x 3.68 m) 800-W module, and we are developing associated module production equipment that will minimize the total installed system cost for utility-scale PV arrays. Activities in Phase 2 focused on the development of automation for module materials lay-up, cell string busing, and module lamination; enhancements to the cell stringing and lamination processes; and performance testing of large-area modules.

15. SUBJECT TERMS
PV; automated production line processes; modules; manufacturing; large area; utility-scale; high-volume; cell string busing; lamination; scale-up

16. SECURITY CLASSIFICATION OF:			17. LIMITATION OF ABSTRACT	18. NUMBER OF PAGES	19a. NAME OF RESPONSIBLE PERSON
a. REPORT	b. ABSTRACT	c. THIS PAGE			
Unclassified	Unclassified	Unclassified	UL		19b. TELEPHONE NUMBER *(Include area code)*